AGU PUBLICATIONS

JGR

Journal of Geophysical Research: Solid Earth

RESEARCH ARTICLE
10.1002/2016JB013646

Key Points:
- The onset of crack damage is a function of increasing differential stress, regardless of whether mean stress is increasing or decreasing
- The intermediate principal stress then controls the amount of crack damage that ensues and preferentially aligns cracks, but mean crack size remains the same
- Cyclic stressing shows that the transition from elastic to inelastic behavior (damage envelope) is dynamic and evolves with stress level

Supporting Information:
- Supporting Information S1

Correspondence to:
J. Browning,
j.browning@ucl.ac.uk

Citation:
Browning, J., P. G. Meredith, C. E. Stuart, D. Healy, S. Harland, and T. M. Mitchell (2017), Acoustic characterization of crack damage evolution in sandstone deformed under conventional and true triaxial loading, *J. Geophys. Res. Solid Earth*, *122*, doi:10.1002/2016JB013646.

Received 12 OCT 2016
Accepted 2 JUN 2017
Accepted article online 5 JUN 2017

Acoustic characterization of crack damage evolution in sandstone deformed under conventional and true triaxial loading

J. Browning[1], P. G. Meredith[1], C. E. Stuart[1], D. Healy[2], S. Harland[2], and T. M. Mitchell[1]

[1]Department of Earth Sciences, University College London, London, UK, [2]School of Geosciences, University of Aberdeen, Aberdeen, UK

Abstract We present a comparative study of crack damage evolution in dry sandstone under both conventional ($\sigma_1 > \sigma_2 = \sigma_3$), and true triaxial ($\sigma_1 > \sigma_2 > \sigma_3$) stress conditions using results from measurements made on cubic samples deformed in three orthogonal directions with independently controlled stress paths. To characterize crack damage, we measured the changes in ultrasonic compressional and shear wave velocities in the three principal directions, together with the bulk acoustic emission (AE) output contemporaneously with stress and strain. We use acoustic wave velocities to model comparative crack densities and orientations. In essence, we create two end-member crack distributions; one displaying cylindrical transverse isotropy (conventional triaxial) and the other planar transverse isotropy (true triaxial). Under the stress conditions in our experiments we observed an approximately fivefold decrease in the number of AE events between the conventional and true triaxial cases. When taken together, the AE data, the velocities, and the crack density data indicate that the intermediate principal stress suppresses the total number of cracks and restricts their growth to orientations subnormal to the minimum principal stress. However, the size of individual cracks remains essentially constant, controlled by the material grain size. Crack damage is only generated when the differential stress exceeds some threshold value. Cyclic loading experiments show that further damage commences only when that previous maximum differential stress is exceeded, regardless of the mean stress, whether this is achieved by increasing the maximum principal stress or by decreasing the minimum principal stress.

1. Introduction

All crustal rocks contain some finite void space comprising pores and cracks, and the geometry of the void space is altered by the application of stress, resulting in changes in the rock physical properties. In particular, the presence of microcracks reduces the velocity of acoustic compressional (*P*) and shear (*S*) waves in rocks [e.g., *Sayers et al*., 1990]. Under hydrostatic compression, these cracks are elastically closed, causing acoustic velocities to increase isotropically, provided that the rock is initially isotropic [*Hadley*, 1976]. By contrast, where differential stresses are applied, elastic crack deformation (closure, opening, or by shear displacement) becomes anisotropic, and the related changes in acoustic wave velocities are therefore also anisotropic [*Nur and Simmons*, 1969; *Soga et al*., 1978; *Sayers et al*., 1990; *Sayers and Van Munster*, 1991; *Stuart et al*., 1993; *Crawford et al*., 1995; *Schubnel et al*., 2003; *Ghaffari et al*., 2014; *Nasseri et al*., 2014]. Such anisotropy will be generated under conventional triaxial stress ($\sigma_1 > \sigma_2 = \sigma_3$), as applied in the vast majority of experimental studies, but will be further enhanced under true triaxial stress ($\sigma_1 > \sigma_2 > \sigma_3$), as is the general case in the crust [*Zoback and Zoback*, 2002].

Under sufficiently high differential stress, new crack damage is generated by inelastic processes in rocks of all types and such cracking is identifiable through the output of acoustic emissions [*Cox and Meredith*, 1993]. The new crack damage also causes acoustic wave velocities to decrease [*Lockner et al*., 1977; *Sayers and Van Munster*, 1991], due to the increased crack porosity. In some cases these new cracks have a highly anisotropic orientation distribution, and the resulting changes in acoustic wave velocities are therefore also highly anisotropic. This anisotropy can be measured using an array of velocity transducers and by measuring *P* and *S* wave velocities concurrently [*Schubnel et al*., 2006; *Ghaffari et al*., 2014; *Nasseri et al*., 2014; *Brantut*, 2015]. While elastic opening and closure of microcracks is, by definition, reversible, inelastic processes will result in permanent changes to the void space (pores and cracks), and therefore permanent changes in the wave velocities [*Han*, 2016]. In low porosity rocks (e.g., crystalline rocks such as granites or basalts) these

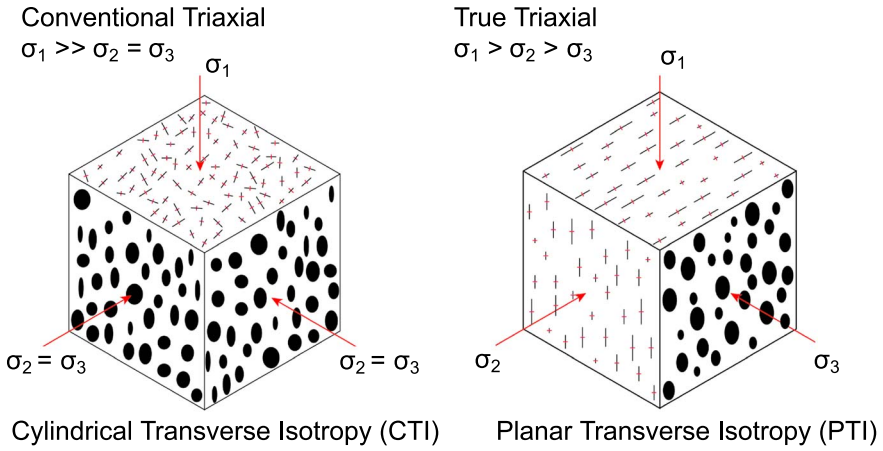

Figure 1. Schematic diagram showing the distribution of cracks formed during conventional triaxial and true triaxial loading: (a) conventional triaxial tests where microcrack populations are expected to display cylindrical transverse isotropy (CTI); (b) true triaxial tests where microcracks are expected to display planar transverse isotropy (PTI).

changes generally involve dilatant crack growth and velocity decrease. In rocks with high intergranular porosity (e.g., sedimentary rocks such as sandstones), velocities can either increase or decrease due to the competition between grain crushing and pore collapse and dilatant crack growth [*Baud et al*., 2012].

Considerable theoretical work has been performed on the elastic properties of solids containing cracks, and this has been widely applied to rock properties [e.g., *Anderson et al*., 1974; *Hoenig*, 1979; *Sayers and Kachanov*, 1995; *Han*, 2016]. An important approach to modeling within this theoretical framework is to use an effective medium model, in which each crack in the solid medium is regarded as being embedded in a solid with the overall properties of the cracked body [*Kachanov*, 1992; *Sayers and Kachanov*, 1995]. At very high loads (close to the peak stress), the crack density becomes sufficiently high that crack interaction and coalesence inevitably occurs, which is also a precursor to ultimate failure [*Lockner*, 1993; *Wibberley et al*., 2007; *Ingraham et al*., 2013; *Healy et al*., 2015].

It has previously been demonstrated that under true triaxial stress conditions, the intermediate principal stress plays a crucial role in controlling rock strength, with significantly higher differential stresses being required to reach failure as the intermediate principal stress is increased [*Haimson and Chang*, 2000; *Haimson*, 2006]. Since brittle failure results from the coalesence and localization of crack damage [*Lockner*, 1993], it follows that the evolution of anisotropic crack damage may provide an explanation for this phenomenon. However, a systematic study of this process has yet to be presented. We therefore report results from an experimental investigation that directly compares crack damage evolution in conventional triaxial tests with that in truly triaxial tests. Additionally, we have performed cyclic loading experiments that have allowed us to discriminate between the elastic opening and closing of preexisting cracks and the inelastic opening of new cracks (i.e., new crack damage). We use AE measurements to detect the initiation and growth of new crack damage, in combination with acoustic *P* and *S* wave velocity measurements along orthogonal directions to measure the anisotropic closure and/or opening of cracks. Taken together, these measurements allow us to model evolving crack densities and estimate mean crack sizes under both conventional and true triaxial stress states.

We represent cracks in the samples deformed under conventional triaxial stresses using the method of *Sayers and Kachanov* [1995] where changes in elastic wave velocities are used to calculate a compliance tensor which is then converted to a crack density tensor via the elastic moduli. In this case the crack population displays cylindrical transverse isotropy (CTI) (Figure 1a), in which cracks are isotropically distributed around the plane normal to the maximum principal stress (σ_1), giving two independent crack populations, N_1 and N_3, and two concomitant crack densities α_1 and α_3. By contrast, for the samples deformed under true triaxial stress we have extended the *Sayers and Kachanov* [1995] model, following a similar approach to that of *Guéguen and Kachanov* [2011], in order to obtain three independent crack populations, N_1, N_2, and N_3, and three crack

densities α_1, α_2, and α_3, which each displays planar transverse isotropy (PTI) (Figure 1b), and where cracks are preferentially oriented normal to the minimum principal stress (σ_3).

In parallel with the elastic wave velocity measurements we also measured the output of AE to characterize new crack damage. In particular, we have used the onset of AE to pinpoint the onset of new crack damage during cyclic stressing experiments. The onset of new damage, and AE, on any loading cycle marks the boundary between elastic and inelastic deformation. However, following their inelastic formation, new cracks can close elastically on unloading and then reopen elastically in subsequent loading cycles. This has important consequences because, as previously shown by *Holcomb and Costin* [1986], it means that the elastic-inelastic boundary (which we hereinafter refer to as the *damage envelope*) is not fixed but can move whenever the differential stress exceeds its previous maximum and extra crack damage is accumulated.

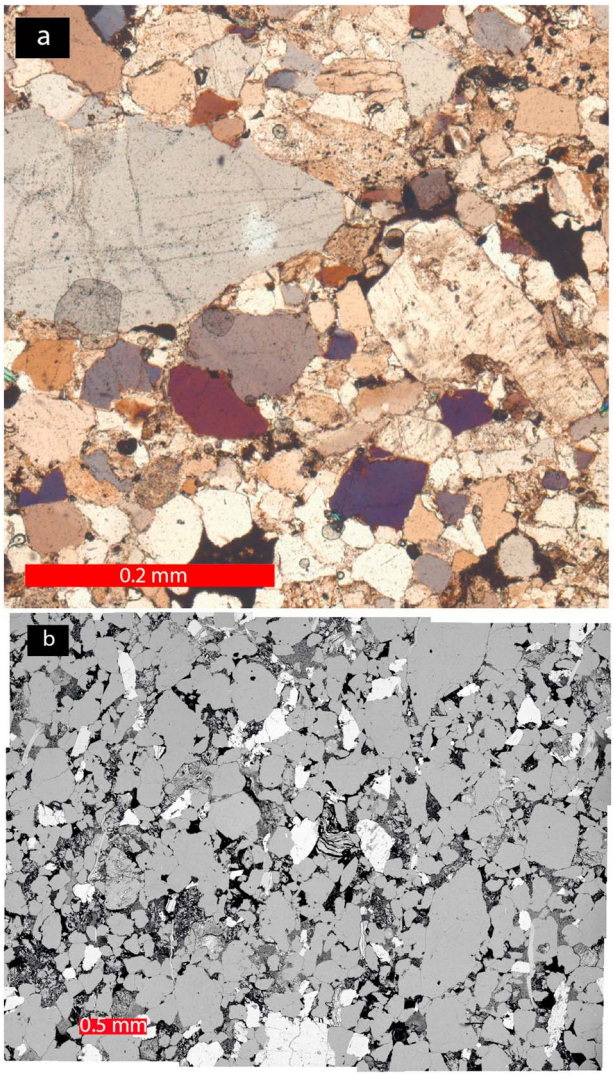

Figure 2. Optical (a) and scanning electron microscope in backscatter electron mode (b) images of undeformed Darley Dale sandstone.

2. Experimental

2.1. Materials and Methods

All experiments in this study were carried out at room temperature on dry samples of Darley Dale sandstone, a feldspathic sandstone with a moderate porosity of ~13% [*Heap et al.*, 2009a; *Wu et al.*, 2000]. It has a mean grain size of 0.4 mm [*Hackston and Rutter*, 2016] with a grain size range from 0.08 to 0.8 mm (Figure 2). This rock was chosen because it is a well-studied and well-characterized material with a void-space microstructure comprising both pores and cracks. We manufactured cubic samples with an edge length of 50 mm (±0.03 mm) and with opposing faces ground flat and parallel to within ±0.0 l mm. The starting material is essentially homogeneous and has a *P* wave velocity anisotropy of ~10%, which classifies it as weakly anisotropic [*Thomsen*, 1986]. This originates from a weak grain shape fabric parallel to bedding [*Hackston and Rutter*, 2016]. We therefore used the bedding plane, measured ultrasonically, to define the principal loading directions, with σ_{11} normal to and σ_{22} and σ_{33} parallel to bedding (Figure 4a).

The deformation apparatus used for all experiments was based at the laboratories of Koninklijke/Shell Exploratie en Produktie Laboratoriu (KSEPL), Rijswijk, Netherlands. Samples were deformed in a three-axis stressing frame constructed of flanged steel beams, one of which was removable to allow the insertion of the sample (Figure 3). Three pairs of servocontrolled hydraulic rams with a loading capacity of 300 kN and hemispherical seatings were used to provide the loads along orthogonal axes perpendicular to the faces of the samples, via loading platens interposed between the rams and the sample faces to provide the contact surfaces. In order to load in three orthogonal directions simultaneously, it is necessary for the platen face area

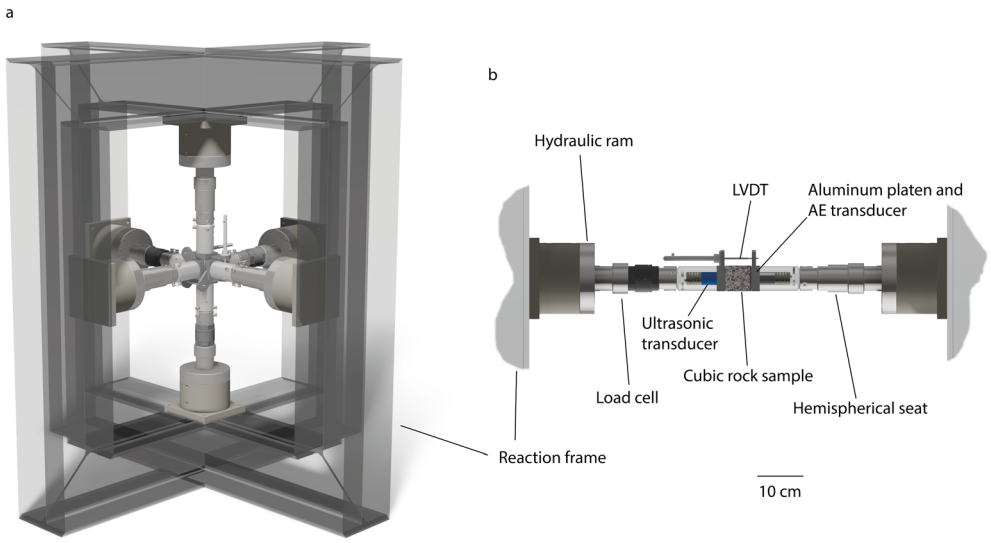

Figure 3. (a) Schematic of the true triaxial loading apparatus used in the experiments with (b) detailed schematic of the sample loading configuration.

to be smaller than the cross-sectional area of the sample and so each platen had an edge length of 47.5 mm. Aluminum was chosen as the platen material to match the elastic properties of our sample material as closely as possible in order to minimize edge effects. Earlier studies have reported finite element modeling to simulate the distribution of stress within cubic samples loaded in this way [e.g., *Stuart*, 1992; *Shi et al*., 2012]. Although high stress gradients were observed locally at the sample edges and corners, *Stuart* [1992] found a highly uniform stress distribution throughout the bulk of the sample when elastic properties were matched in this way. Prior to each deformation experiment, a small preload of 4 MPa was applied along each of the three axes to keep the sample centered within the apparatus and to ensure good acoustic contact between the sample and the loading platens. The load in each of the three directions was measured using electronic load cells with 300 kN capacity and an accuracy of ±0.2%, and the displacement in each direction was measured using linear variable differential transformers (LVDTs) mounted between the loading platens (Figure 3). Pairs of acoustic velocity transducers were mounted in holders directly behind each platen allowing three *P* wave velocities and three *S* wave velocities to be recorded simultaneously, as illustrated in Figure 3. Additionally, an AE transducer was located in a recess within one of the platens. Load (stress), displacement (strain), and compressional (*P*) and shear (*S*) wave

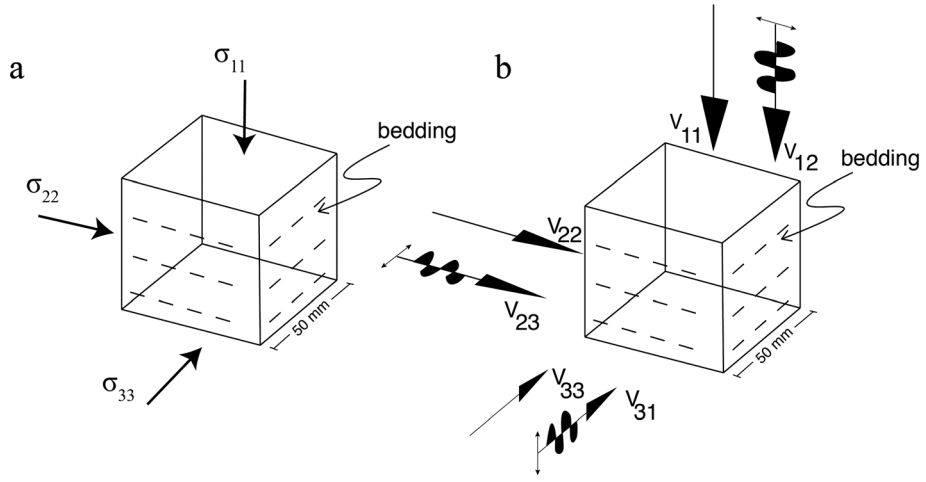

Figure 4. Reference frames and nomenclature for (a) principal stress orientations and (b) acoustic *P* wave propagation (compressional) and *S* wave polarization (shear) directions, with respect to a cubic bedded sample with sides of 50 mm length.

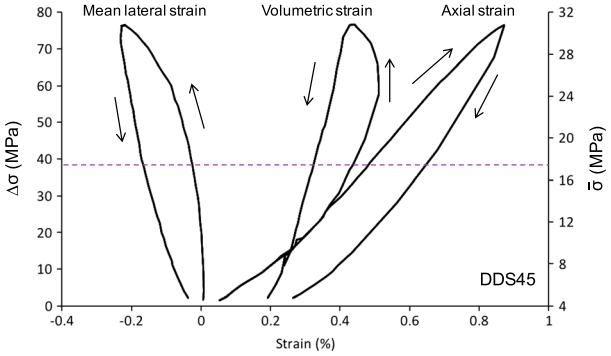

Figure 5. Stress-strain curves for the conventional triaxial compression test ($\sigma_2 = \sigma_3 = 4$ MPa, σ_1 variable). The dashed purple line indicates the onset of dilatancy as observed from AE and ultrasonic velocities. $\Delta\sigma$ is differential stress ($\sigma_1 - \sigma_3$) and $\bar{\sigma}$ is mean stress ($(\sigma_1 + \sigma_2 + \sigma_3)/3$).

travel times, measured in the three orthogonal directions, were logged contemporaneously at predetermined intervals (50 s) during each test, and AE were recorded continuously between these logging periods.

The *P* and *S* wave transducers had a nominal frequency of 1 MHz, giving a dominant wavelength of ~3.5 mm, significantly larger than the grain size of Darley Dale sandstone (0.08–0.8 mm), and significantly smaller than the sample dimension (50 mm). The nominal resonant frequency of the AE transducer was 0.5 MHz. The arrival times of AE wave packages (hits) were used to calculate AE hit rate and the cumulative number of hits as a function of time (see *Cox and Meredith* [1993], for a detailed description of the AE recording method and analysis).

2.2. Experimental Protocol

In order to characterize the loading and velocity measurements with respect to the axes of the cubic sample, we define σ_{11} as the direction of the maximum principal compressive stress (σ_1), and σ_{22} and σ_{33} as those of the intermediate (σ_2) and minimum (σ_3) principal stresses in all true triaxial tests (Figure 4). In conventional triaxial tests, σ_{22} and σ_{33} are equal, and also equal to σ_2 and σ_3. In the tests described throughout, the maximum stress is always normal to the previously defined bedding plane, whereas the intermediate and minimum stresses are both parallel to this plane (Figure 4a). The acoustic wave type nomenclature, based on the same set of orthogonal axes, employs two suffixes *i* and *j* (as in V_{ij}) where *i* refers to the propagation direction of the wave, and *j* refers to the particle motion or polarization direction. The propagation and polarization indices *i* and *j* take the values 1, 2, or 3 in accordance with the relevant stress direction. Thus, V_{11} is the velocity of the *P* wave in the direction of the maximum principal compressive stress, and V_{12} is the velocity of the *S* wave propagating in the same direction, but polarized in the 1–2 plane (Figure 4b).

In the first series of tests, σ_{22} and σ_{33} were both set equal and constant at 4 MPa, while σ_{11} was increased; so a condition of cylindrical symmetry existed. Thus, $\sigma_1 > \sigma_2 = \sigma_3$, which approximates to the case of conventional triaxial tests that use cylindrical samples and a fluid as the confining pressure medium. In this case, new cracks are formed with their major (*a*) axes predominately parallel to σ_{11}, and their minor (*c*) axes approximately orthogonal to this direction. The anisotropy resulting from these cracks is cylindrical transverse isotropy (CTI) [*Hoenig*, 1979]. In the case of the preexisting cracks a more general type of transverse isotropy is formed under the differential loading, which can be represented as a sum of planar transverse isotropies (PTIs) [*Hoenig*, 1979] due to the closure of cracks with *c* axes parallel to σ_{11} and CTI due to the elastic opening of cracks with *c* axes lying parallel to σ_{22} and σ_{33}.

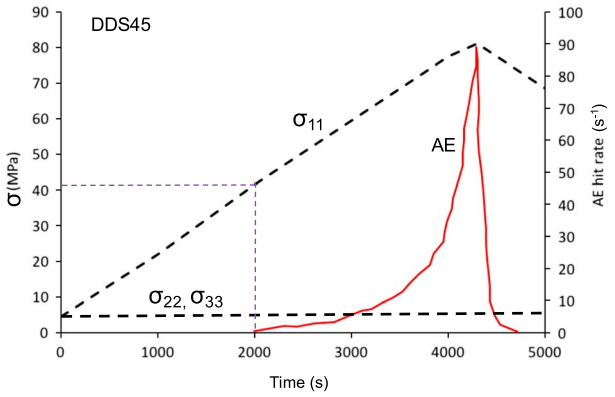

Figure 6. Acoustic emission (AE) data from the conventional triaxial test with AE hit rate (red line) as a function of increasing stress. The dashed purple line indicates the onset of AE.

In the second and third series of tests, the applied stresses were varied either cyclically or at different rates in order to investigate the Kaiser stress memory effect [*Holcomb*, 1993; *Lockner*, 1993; *Lavrov*, 2001] and the particular influences of differential stress and mean

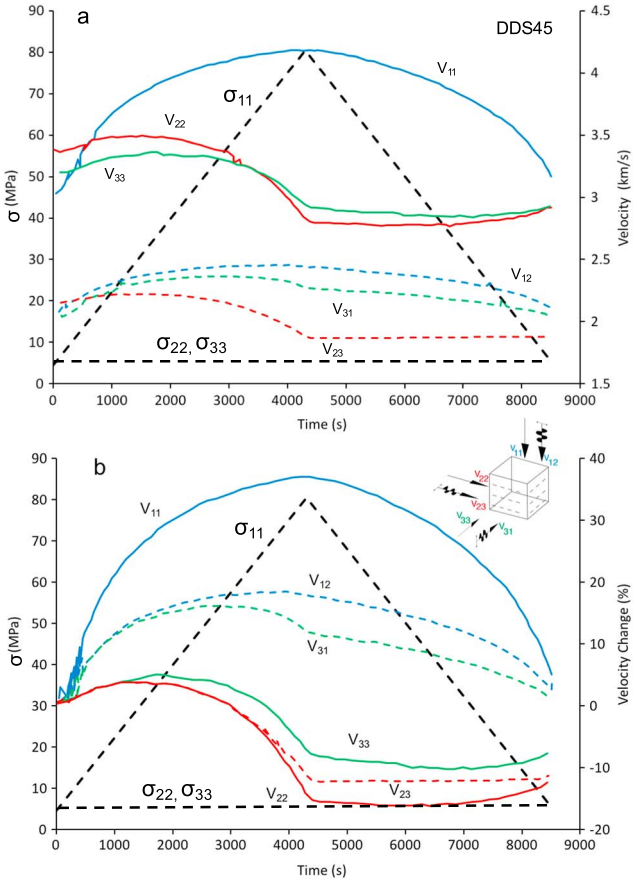

Figure 7. Acoustic wave velocity data from the conventional triaxial compression test. (a) Velocities of elastic compressional waves (solid lines) and shear waves (dashed lines) as a function of stress (black dashed lines). (b) Percentage changes in elastic compressional (*P*) and shear (*S*) wave velocities with stress (black dashed line).

stress on crack growth and closure. In both series of tests, σ_{22} and σ_{33} were again maintained equal ($\sigma_1 > \sigma_2 = \sigma_3$).

In the final series of tests, the intermediate principal stress differed from the other principal stresses to produce a truly triaxial stress state where $\sigma_1 > \sigma_2 > \sigma_3$. In this case, new cracks are formed with their minor (*c*) axes parallel or subparallel to σ_3 (= σ_{33}). This gives rise to PTI with the axis of symmetry parallel to σ_{33}. Simultaneously, closure of preexisting cracks with *c* axes parallel to σ_{11} and σ_{22} produces PTI with axes of symmetry parallel to σ_{11} and σ_{22}, respectively.

Below we present detailed results from representative experiments from each of the four series. Overall, a total of 24 experiments were performed and a table listing the experimental conditions for all experiments is given in the supporting information (Table S1). The experiment number is given on all data figures in the following sections so that the reader can refer to the detailed conditions of each experiment in Table S1.

3. Experimental Results

3.1. Conventional Triaxial Stress (Cylindrical Transverse Isotropy)

In the conventional triaxial tests, σ_{11} was increased at a rate of 0.018 MPa/s to a maximum value of 81 MPa (approximately 80% of the conventional triaxial compressive strength of Darley Dale sandstone at a confining pressure, P_c = 4 MPa) and then unloaded at the same rate. Loading in the other directions was both equal and constant, where $\sigma_{22} = \sigma_{33}$ = 4 MPa. The resulting stress-strain curves are shown in Figure 5 where the strains are plotted against both differential stress ($\Delta\sigma = \sigma_{11} - \sigma_{33}$) and mean stress ($\overline{\sigma} = (\sigma_{11} + \sigma_{22} + \sigma_{33})/3$). In particular, the volumetric strain curve shows that net dilatancy (i.e., the point where dilatancy exceeds elastic compaction) occurs at stresses above ~60 MPa. Therefore, the onset of inelastic (dilatant) crack growth must occur earlier in the deformation. Dilantancy is defined as the deviation from linearity of the volumetric strain curve, but visual inspection of Figure 5 shows clearly that none of the three strain curves exhibits any linear portion. This is a common observation during deformation of porous sandstones, and *Holcomb and Costin* [1986] have pointed out that under these circumstances, the onset of dilantancy cannot be easily determined from the stress-strain data alone. We therefore adopt the pragmatic approach of using the wave velocity data and the AE data to guide us in determining this point. Figure 7b shows that the velocities of *P* waves orthogonal to σ_{11} (V_{22} and V_{33}) and of *S* waves polarized in the plane normal to σ_{11} (V_{23}) all initially increase, peak at a stress around 40 MPa, and subsequently decrease (for comparison, the same data are shown plotted against stress in Figure S1). By contrast, the *P* wave velocity in the σ_{11} direction (V_{11}) shows no clear evidence of any new crack damage, with the increase during loading and decrease during unloading being essentially identical. However, while the velocities of shear waves polarized in planes containing σ_{11} (V_{31} and V_{12}) do not peak at the same point, they do show clear evidence of the occurrence of cracking by peaking before the maximum stress and close to the onset of net dilatancy. Taken together, these observations are consistent

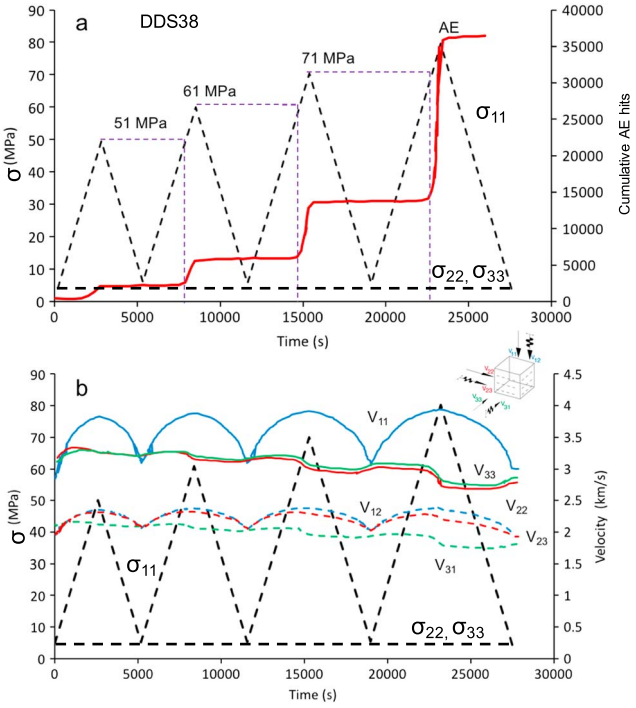

Figure 8. Evidence of the Kaiser stress-memory effect during cyclic conventional triaxial compression test. (a) Variation of cumulative AE hits and (b) variation of compressional (solid lines) and shear (dashed lines) wave velocities with σ_{11}.

and suggest that the onset of dilatant cracking commences around 40 MPa. This onset is confirmed by our AE data in Figure 6 which shows that significant AE output also commences around 40 MPa. We therefore use the onset of significant AE as an indicator of the onset of dilatant crack damage in our experiments.

Following its onset, inelastic cracking increases as long as the stress continues to increase but also continues to be accompanied by crack closure due to increasing σ_{11}. In the case of waves propagating in the σ_{22} direction (V_{22} and V_{23}), inelastic crack growth eventually dominates, causing a permanent reduction in velocity above a stress of ~55 MPa. Similarly, the *P* waves propagating in the σ_{33} direction (V_{33}) show a predominance of inelastic crack growth once the stress exceeds ~62 MPa. These events appear to be correlated with the peaks in V_{31} and V_{12}, respectively (Figure 7).

The AE data (Figure 6) support this interpretation. After onset, the AE rate increases quasi-exponentially while loading increases linearly. But immediately upon unloading, the AE rate drops dramatically reaching zero after a very short time. This rapid drop suggests that the unloading processes are entirely, or at least primarily, elastic. Elastic reopening of previously elastically closed cracks causes a small continuing reduction of velocity as σ_{11} is reduced, but eventually at stresses below ~40 MPa elastic closure of the cracks causes an increase in velocity. In the case of the shear waves polarized in the direction of σ_{11} (V_{12} and V_{31}) the effect of the elastic reopening is relatively large, and it dominates over effects due to inelastic cracking, such that these velocities recover their initial values once the differential load on the sample is reduced to zero. The relative magnitudes of the velocity changes for the various acoustic waves show the high degree of anisotropy caused by the elastic and inelastic deformations under stress. Inelastic crack growth is predominantly orthogonal to the main elastic crack closure (compare V_{22}, V_{33}, and V_{23} to V_{11}). Although loading is identical in the σ_{22} and σ_{33} orientations, there is a small difference between the changes in V_{22} and V_{33}. This is due to differences in the initial elastic properties of the rock between these two directions. In the case of shear waves with polarization planes containing σ_{11}, the competing effects of elastic crack closure and inelastic crack growth offset each other to a large extent.

3.2. Cyclic Conventional Triaxial Stress (Kaiser Stress-Memory Effect)

The division of cracks into elastic and inelastic contributions to the overall deformation was confirmed by cyclically stressing a sample to increasingly elevated peak stress levels. The AE results from these tests highlight the Kaiser stress-memory effect [*Lockner*, 1993; *Stuart et al.*, 1995] (Figure 8a), whereby AE is only observed in any cycle once the maximum stress in the previous cycle (σ_{11} in this case) has been exceeded. During unloading, existing cracks close elastically, and these same cracks then reopen elastically during reloading on the next cycle. Only when the previous maximum stress is exceeded, is new crack damage generated.

Both elastic crack reopening and inelastic crack growth, which produces the observable AE, can be seen in the wave velocity data (Figure 8b). The *P* wave velocity parallel to σ_{11} (V_{11}) shows a predominantly elastic response throughout all loading and unloading cycles with the maximum velocity increasing slightly with each increasing maximum stress as more cracks become closed. By contrast, V_{22} and V_{33} do not exhibit any velocity recovery during unloading but instead decrease gradually with each increasing maximum

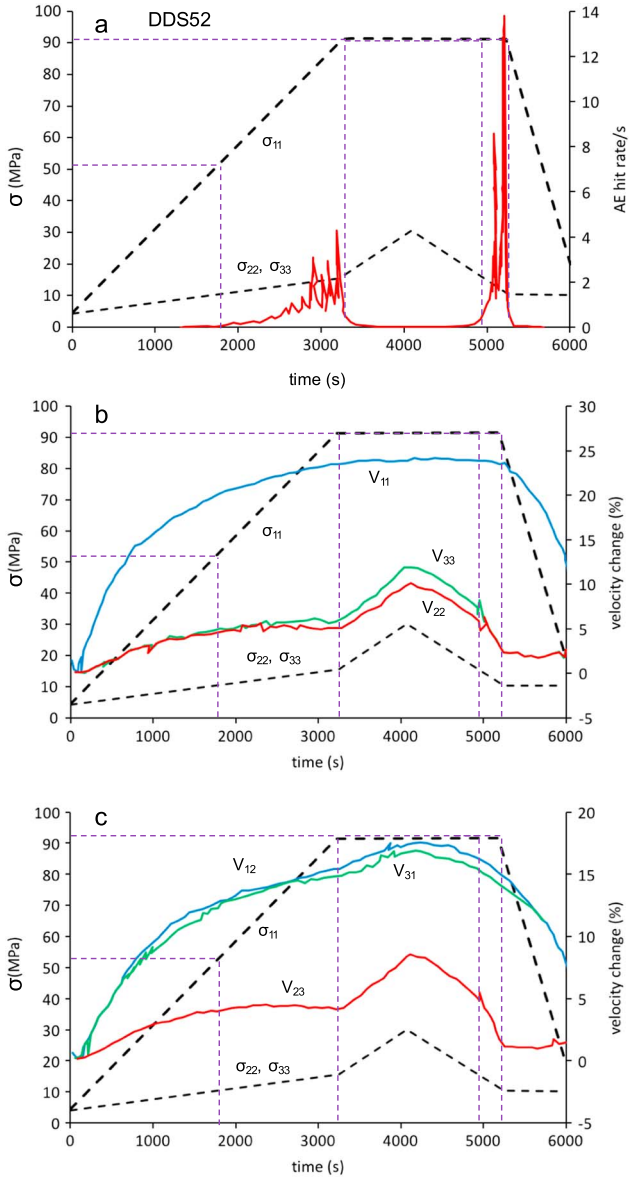

Figure 9. AE and acoustic wave output during a varied conventional triaxial stress loading and unloading path. Variation of (a) AE hit rate, (b) V_p, and (c) V_s with time.

stress as new cracks grow in these directions. The *S* wave velocities generally support the *P* wave velocities in highlighting the presence of both elastic opening/closure and inelastic crack growth, with V_{12} and V_{31} exhibiting essentially elastic behavior while V_{23} exhibits inelastic behavior (in a similar manner to V_{22} and V_{33}).

The generation of increased levels of AE activity with each increase in maximum stress level during cyclic loading is associated with an increase in the number of new cracks; that is, an increase in the level of crack damage within the sample. This implies that we can use the onset of AE during loading to differentiate between states of stress where damage is constant and states of stress where damage is increasing [*Holcomb and Costin*, 1986]. We can therefore define a *damage envelope*, as the boundary in stress space that can be reached without inducing further damage, analogous to a failure envelope which defines the boundary in stress space that can be reached before failure occurs. Furthermore, it is clear from the data of Figure 8a that the damage envelope is not a fixed boundary but is dynamic. During successive loading cycles the onset of AE occurs at increasing levels of stress, suggesting that the damage envelope is being pushed ever closer toward the failure envelope.

3.3. Conventional Triaxial Stress (Differential Versus Mean Stress)

The importance of differential stress in relation to mean stress in controlling crack growth was investigated in a series of tests where σ_{11}, σ_{22}, and σ_{33} were changed at different rates during a number of loading and unloading paths in order to explore the relation between the stress state and the damage envelope (Figure 9).

In the first stress path, σ_{11} was increased from 4 to 92 MPa at a rate of 0.0280 MPa/s, while σ_{22} and σ_{33} were simultaneously increased from 4 to 15 MPa at 0.0035 MPa/s. During this path, AE output commenced when σ_{11} reached 52 MPa, corresponding to a differential stress ($\sigma_{11} - \sigma_{33}$ (= σ_{22})) of about 42 MPa, very close to the value for the onset of AE in the conventional triaxial test of Figure 6. The AE output then increased quasi-exponentially as differential stress was increased to its maximum value of 77 MPa (σ_{11} = 92 MPa and $\sigma_{22} = \sigma_{33}$ = 15 MPa).

In the second stress path, σ_{11} was held constant at 92 MPa while σ_{22} and σ_{33} were simultaneously increased at a higher rate of 0.016 MPa/s to 30 MPa. Figure 9a shows that the AE output ceases immediately, indicating

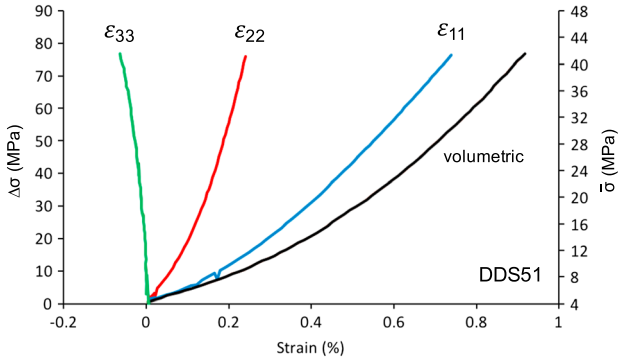

Figure 10. True triaxial test stress-strain curves. $\Delta\sigma$ is differential stress ($\sigma_1 - \sigma_3$) and $\bar{\sigma}$ is mean stress ($(\sigma_1 + \sigma_2 + \sigma_3)/3$).

a concomitant cessation of cracking. This occurs because the differential stress is decreasing, even though the mean stress is actually increasing.

In path three, σ_{22} and σ_{33} were both decreased at the same rate of 0.016 MPa/s while σ_{11} was again held constant at its maximum value, thus increasing the differential stress while simultaneously decreasing the mean stress. Under these conditions, we observe a very abrupt recommencement of AE output at the exact point where the differential stress exceeds its previous maximum level. In essence, this is a manifestation of the Kaiser effect (indicating the onset of new crack damage) during unloading conditions and demonstrates that it is the differential stress rather than the overall stress state that governs the onset and nucleation of new cracks. We subsequently observe a supraexponential increase in AE output as the differential stress is increased further when σ_{22} and σ_{33} are reduced to 10 MPa.

In the final path, σ_{11} was decreased while σ_{22} and σ_{33} were maintained constant at 10 MPa, thus again reducing the differential stress. Again, we observe an immediate and abrupt cessation of AE, indicating a commensurate cessation in cracking.

Taken together, these observations demonstrate conclusively that the onset of new crack damage depends exclusively on the level of differential stress, rather than on the level of mean stress or maximum stress. We discuss later the relation between differential stress and mean stress in controlling the amount of new crack damage.

Observations of the changes in *P* and *S* wave velocities, illustrated in Figures 9b and 9c, entirely support and complement the AE data. However, the onset of new, inelastic crack damage at σ_{11} = 52 MPa is not as clearly seen in the velocity curves, because preexisting cracks are still closing at the same time as new cracks are opening. But we note that the *P* wave velocities normal to the maximum stress direction (V_{22} and V_{33}), and hence normal to the new cracks, stop increasing with increasing differential stress and then start to decrease as the maximum differential stress is approached. A similar pattern is seen in the *S* wave velocity propagating and polarized normal to the σ_{11} direction (V_{23}).

When the differential stress is decreased by raising the values of σ_{22} and σ_{33}, we see an immediate and substantial increase in all the velocities (except V_{11}, as expected) due to elastic closure of cracks. This trend is immediately reversed when σ_{22} and σ_{33} are decreased such that the differential stress increases and the cracks elastically reopen. Further to this, when the previous maximum differential stress is exceeded, and we observe a rapid acceleration in AE (Figure 9a), we also see a simultaneous increase in the rate of velocity decrease in V_{22}, V_{33}, and V_{23}, commensurate with the recommencement of new crack damage.

Finally, during unloading (decrease in σ_{11}), we observe essentially no change in V_{22}, V_{33}, and V_{23}, as expected, while we simultaneously observe substantial decreases in all velocities propagating or polarized parallel to σ_{11} (V_{11}, V_{12}, and V_{31}), as horizontal cracks that were previously elastically closed by σ_{11} start to reopen.

3.4. True Triaxial Stress (Planar Transverse Isotropy)

The stress-strain curves from one of our series of true triaxial tests are shown in Figure 10. Here we again fixed σ_{33} but increased σ_{22} at a rate that was 50% of the increase in σ_{11} (note that throughout these tests, $\sigma_{11} = \sigma_1$, $\sigma_{22} = \sigma_2$, and $\sigma_{33} = \sigma_3$), hence when σ_1 increases from 4 MPa to 82 MPa, σ_2 increases from 4 MPa to 43 MPa, while σ_3 remains constant at 4 MPa. As expected, the volumetric strain curve shows only a small amount of overall dilatancy and no net dilatancy, since the stress difference between σ_1 and σ_2 never exceeds 42 MPa which is the minimum differential stress required to nucleate new crack growth (Figures 6 and 9). Hence, any new crack damage is restricted to grow in orientations normal or subnormal to σ_3. Consequently, we observe that the AE hit rate at peak stress in the true triaxial test (Figure 11a) is much lower than that in the conventional

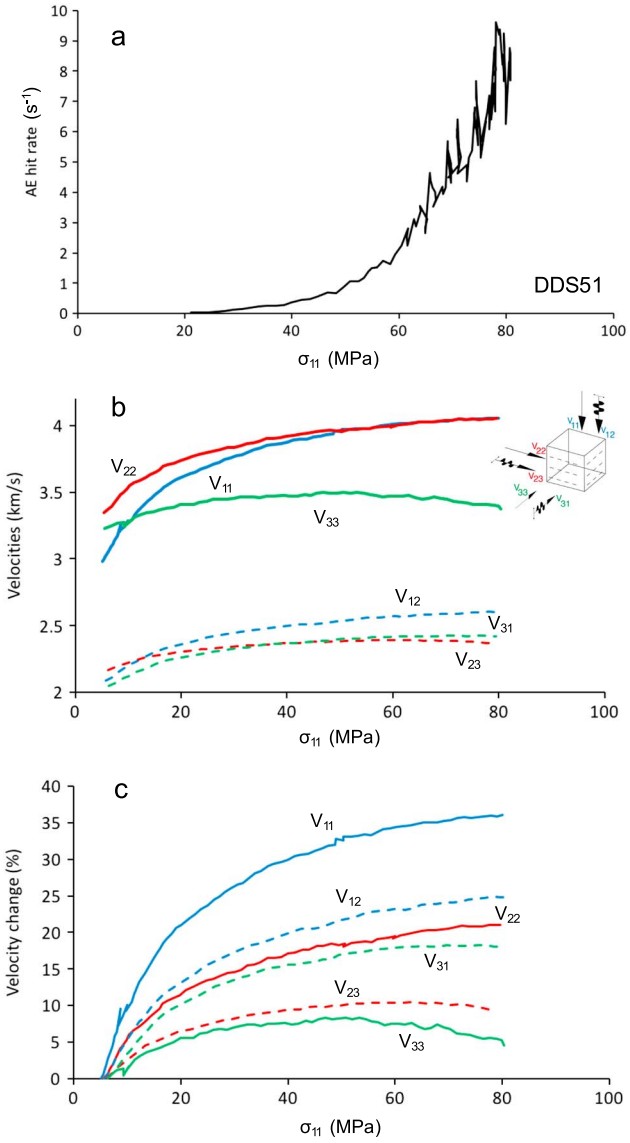

Figure 11. Acoustic data for the true triaxial test. (a) Acoustic emission (AE) hit rate as a function of increasing stress. (b) Velocities of elastic compressional (solid lines) and shear (dashed lines) waves as a function of σ_{11}. (c) Velocity change expressed as percentages.

triaxial test, at about 10%, and the total number of AE hits recorded is also lower than that in the conventional triaxial test, at about 20%.

The *P* wave velocity data clearly confirm that the population of new cracks have a planar transverse isotropic distribution, with *c* axes subparallel to the σ_{33} direction. The changes of V_{11} and V_{22} (Figure 11c) are due to elastic closure of cracks with *c* axes in the σ_{11} and σ_{22} directions, respectively, and it is interesting to note that the relative change in V_{22} is approximately half that of the change in V_{11}, in agreement with the fact that the load in the σ_{22} direction is only half of that in the σ_{11} direction. Oriented crack damage causes V_{33} to peak at a stress of 45–50 MPa, but in this case the dilatancy-induced velocity reduction is much smaller than for the conventional triaxial test (Figure 7b) in agreement with the much reduced AE output (Figure 11a). These interpretations are further supported by the observed complementary changes in the shear wave velocities for the true triaxial case (Figures 11b and 11c). For completeness and for purposes of comparison we have also plotted the velocity data against time to show the change in velocity as a function of all three principal stresses as shown in Figure S3 in the supporting information.

4. Discussion and Analysis

4.1. Quantitative Microcrack Characterization

As noted earlier, we apply the model of *Sayers and Kachanov* [1995] to our results where the change in elastic (acoustic) wave velocity due to each of the crack distributions is defined using a second rank tensor (γ_{ij}) by

$$\gamma_{ij} = \frac{3E_0(2-\nu_0)}{32(1-\nu_0^2)} a_{ij}, \tag{1}$$

where E_0 is the Young's modulus and ν_0 is the Poisson's ratio in a homogenized background medium and α is the crack density in a given direction (*i* and *j*). We use all six sets of velocity data to determine the resulting crack densities. For the conventional triaxial case the velocity data show that both the elastically deforming preexisting crack population and the new crack damage display cylindrical transverse isotropy and can therefore be represented by two independent crack populations, N_1 and N_3, and with two crack densities α_1 and α_3. By contrast, for the true triaxial case, the velocity data suggest three mutually orthogonal PTI distributions

N_1, N_2, and N_3 with associated crack densities α_1, α_2, and α_3, each having their crack minor (*c*) axes normal to their respective PTI plane. For this latter case, application of a compressive stress σ_{11} causes the closure of cracks in the N_1 population (i.e., a decrease in α_1), and a small degree of opening of the cracks in the N_2 and N_3 populations (i.e., an increase in α_2 and α_3). Similar consequences apply independently and additively by the application of compressive stresses σ_{22} and σ_{33} in the orthogonal directions. These deformations are elastic and therefore reversible provided that the cracks remain open and are not subject to frictional tractions. These elastic deformations will occur under both hydrostatic and differential loads. New crack populations only form under conditions of differential loading when the differential stress exceeds some minimum value for the onset of new damage. We model these cracks as a population with minor (*c*) axes in the minimum principal stress ($\sigma_3 = \sigma_{33}$) direction. Once formed, these cracks can also deform elastically.

If we neglect the fourth rank tensor β term in *Sayers and Kachanov* [1995], which they demonstrate to have a negligible effect for dry rock, and assume orthotropic symmetry (where $\alpha_1 \neq \alpha_2 \neq \alpha_3$) for the true triaxial case, then looping through all orientations (i.e., *i*, *j*, and *k* = 1, 2, and 3) we see that

$$\Delta s_{1111} = \alpha_1 \tag{2}$$

$$\Delta s_{2222} = \alpha_2 \tag{3}$$

$$\Delta s_{3333} = \alpha_3 \tag{4}$$

$$\Delta s_{1212} = (\alpha_1 + \alpha_2)/4 \tag{5}$$

$$\Delta s_{1313} = (\alpha_1 + \alpha_3)/4 \tag{6}$$

$$\Delta s_{2323} = (\alpha_2 + \alpha_3)/4, \tag{7}$$

where ΔS_{ijkl} is the tensorial change in compliance due to the crack damage.

In Voight matrix notation [see *Nye*, 1957], we have

$$\Delta S_{11} = \alpha_1 \tag{8}$$

$$\Delta S_{22} = \alpha_2 \tag{9}$$

$$\Delta S_{33} = \alpha_3 \tag{10}$$

$$\Delta S_{44} = 4(\Delta S_{2323}) = (\alpha_2 + \alpha_3) \tag{11}$$

$$\Delta S_{55} = 4(\Delta S_{1313}) = (\alpha_1 + \alpha_3) \tag{12}$$

$$\Delta S_{66} = 4(\Delta S_{1212}) = (\alpha_1 + \alpha_2) \tag{13}$$

In general, $C_{ij} = S_{ij}^{-1}$ where C_{ij} is the 6×6 Voight matrix of elastic stiffness. We calculate C'_{ij} from the measured velocities in the damaged rock using the method of *Sayers and Kachanov* [1995], modified for orthotropic symmetry (see also *Guéguen and Kachanov* [2011]), giving

$$C'_{11} = \rho {V_{11}}^2 \tag{14}$$

$$C'_{22} = \rho {V_{22}}^2 \tag{15}$$

$$C'_{33} = \rho {V_{33}}^2 \tag{16}$$

$$C'_{44} = \rho {V_{23}}^2 \tag{17}$$

$$C'_{55} = \rho {V_{13}}^2 \tag{18}$$

$$C'_{66} = \rho {V_{12}}^2 \tag{19}$$

Using these equations, we can see that

$$\alpha_1 = \left(\frac{1}{C'_{11}}\right) - S^0_{11} \tag{20}$$

$$\alpha_2 = \left(\frac{1}{C'_{22}}\right) - S^0_{22} \tag{21}$$

$$\alpha_3 = \left(\frac{1}{C'_{33}}\right) - S^0_{33}, \tag{22}$$

where S^0_{ij} is the 6×6 Voight compliance matrix of the intact rock.

In summary, in the true triaxial case we have three mutually orthogonal crack distributions with crack densities α_1, α_2, and α_3, each displaying PTI, and the N_1 and N_2 distributions respond only elastically to stress, whereas the N_3 distribution responds elastically in an analogous manner, but also inelastically as new crack damage is formed. In the original cylindrical transverse isotropic model of *Sayers and Kachanov* [1995] which we use to obtain the crack densities for the conventional triaxial test, we obtain two crack densities, α_1 and α_3.

4.2. Application to Conventional Triaxial and True Triaxial Test Results

We now apply these models to evaluate changes in crack density during both the conventional triaxial and the true triaxial tests. The *P* and *S* wave velocity data can be inverted to give the crack densities at any time (i.e., for any stress condition) during the tests as shown in Figures 12a(1) and 12b(1). We first consider the true triaxial case as it is the more complex of the two examples. As expected, only the crack population α_3 shows the occurrence of new crack damage, as the stress increases above ~40 MPa in both cases (Figure 12b(3)). In the PTI case, the change in α_2 is only about half that in α_1, reflecting the fact that $\sigma_2 = 0.5\sigma_1$ (Figure 12b(2)). However, in both cases we find an initial decrease in α_3 which is not accounted for by our model. This effect presumably arises from cracks whose *c* axes are not directly aligned in the σ_{11}, σ_{22}, or σ_{33} orientations. Contrary to the expectation from the model used in our analysis of the experimental results, there was a component of elastic crack closure contributing to the density (α_3) of cracks with *c* axes in the σ_{33} direction. This must arise from the stresses of σ_{11} and σ_{22} since σ_{33} was kept at a constant low value throughout the test. A correction must therefore be made for this effect before the new crack density can be determined (Figures 12a(3) and 12b(3)).

Since this effect is elastic, as are the changes in α_1 and α_2, and since the changes in α_1, α_2, and α_3 are all elastic at stresses below about 40 MPa (as indicated by the AE data), the required correction can be made if we assume that at these low stresses, the changes in the crack densities are linearly proportional to one another.

The differences between the α_3 curve and the scaled α_1 and α_2 curves then give a good estimate of the change in α_3 which is due to new crack damage alone, as also previously observed by *Ayling et al.* [1995]. The α_2 scaling is neglected in the CTI case. In Figure 13 we show the cumulative AE observed in this test with the change in volumetric crack density, from which it can be seen that the cumulative AE is proportional to the density of new crack damage.

4.3. Number, Size, and Orientation of Cracks in Relation to Stress

Rock failure requires a process by which grain-scale cracks link and coalesce to form macroscopic fractures. Under conventional triaxial stress these cracks can grow with their minor (*c*) axes in any orientation in the σ_2, σ_3 plane. By contrast, under true triaxial stress cracks are restricted, by the elevated level of σ_2, to have their *c* axes aligned approximately parallel to σ_3. We noted earlier that the total number of AE hits recorded under conventional triaxial stress was about 5 times higher than that recorded under true triaxial stress. It is therefore reasonable to assume that the number of new cracks is also 5 times higher in the conventional triaxial case. If the new crack damage is distributed isotropically around the σ_2, σ_3 plane, then the fivefold reduction in the true triaxial case suggests that new cracks also grow in the σ_2, σ_3 plane but with their *c* axes restricted to within about ±15° of the σ_3 direction, if restricted orientation is the crack growth limiting factor. However, we also suggest that the numerical ratio of five to one is limited to the specific stress conditions of our experiment and is not a general observation. With respect to the conventional triaxial case, we would always expect new crack damage to be more limited in both extent and orientation under true triaxial stress but would also expect the numerical ratio and restricted angle to be functions of the intermediate principal stress and specifically the difference between σ_2 and σ_3.

The total number of AE events in the conventional triaxial test was ~32,000 (Figure 13a), so the number of AE events per unit volume was ~32,000/$(50 \times 10^{-3})^3$ m^{-3}. The total increase in the dilatant crack density (α_3), determined from acoustic wave velocity measurements, was 0.117 (Figure 13a). If we assume that each new penny-shaped crack produces one detected AE event then from the definition of crack density ($\alpha = n_v a^3$, where n_v is the number of cracks formed per unit volume and *a* is the mean crack radius), we can determine the mean crack radius, which is 0.78 mm. It is, however, well recognized that not all cracks produce a detectable AE signal. *Lockner* [1993] concluded that detectable AE accounts for only ~1% of crack growth, suggesting that AE wave attenuation prohibits the detection of much of the cracking [*McLaskey and Lockner*, 2014]. Assuming the lowest case of a 1% proportionality of detectable AE to cracks then the mean crack radius in our test becomes 0.17 mm. However, it is likely that those cracks which produce detectable

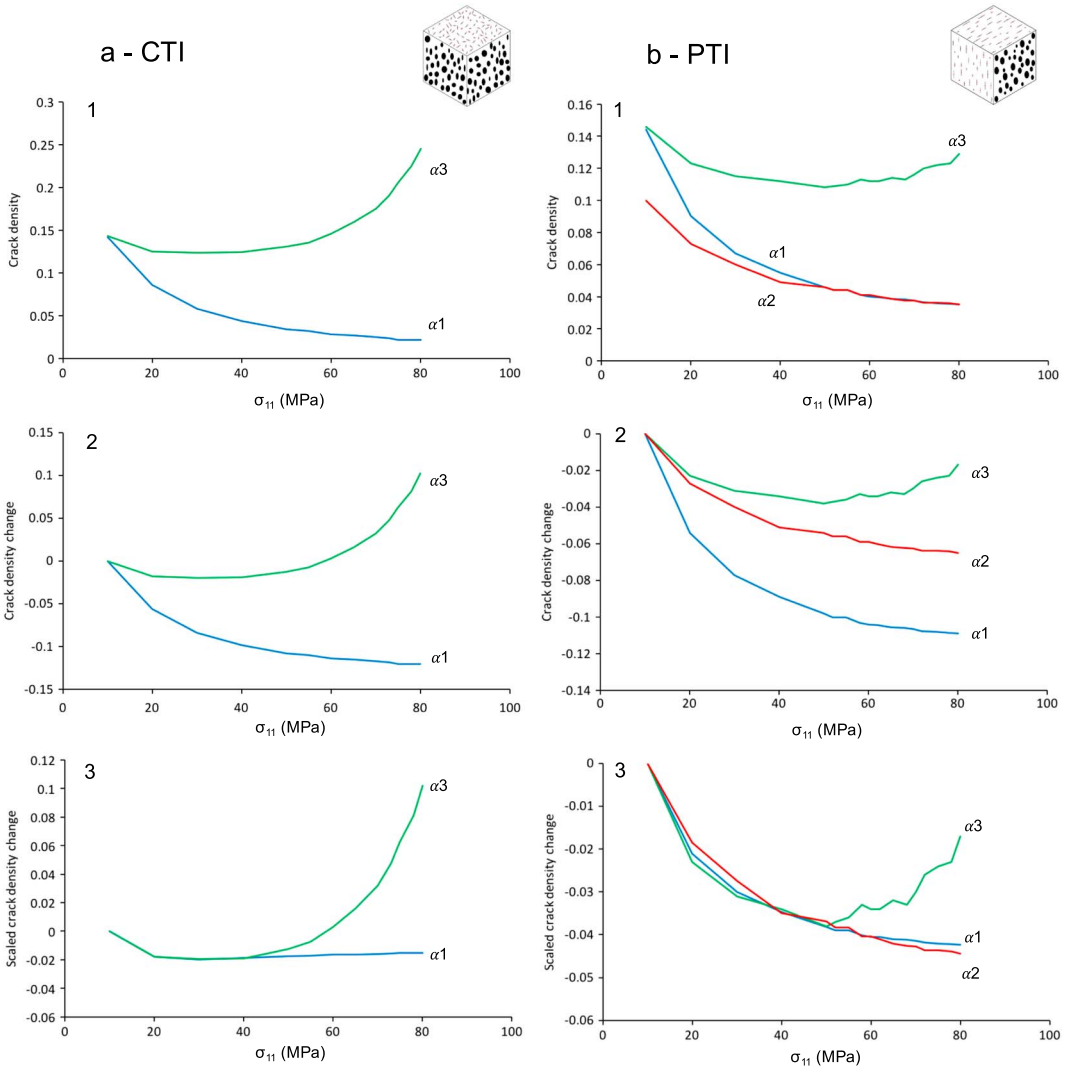

Figure 12. Modeled crack density variables for (a) conventional triaxial stress and (b) the true triaxial compression test. (1) Modeled crack densities calculated from compressional wave and shear wave variations for cracks of different orientations. (2) Changes in crack densities. (3) Calculated crack density changes for cracks of orthogonal orientations (with minor axes in the σ_{11}, σ_{22}, and σ_{33} directions), based on scaling the changes for cracks with σ_{33} orientations to match those with σ_{11} and σ_{22} orientations (see text for fuller explanation).

AE are also those with the largest increments of crack growth. Hence, it is reasonable to take the geometric mean between the extreme 1% and 100% cases. In this case, we find a mean crack radius of 0.36 mm, which fits well to the mean grain size of Darley Dale sandstone.

The total number of AE events in the true triaxial test is roughly 5 times lower than in the conventional triaxial test, at ~6600 (Figure 13b), so the number of AE events per unit volume was ~6600/(50 × l0^{-3})^3 m^{-3}. However, the increase in crack density was also roughly 5 times smaller at 0.026 (Figure 13b). Using the same method as for the conventional triaxial case we find a mean crack radius of 0.79 mm. For the lowest case of a 1% proportionality of detectable AE to cracks then the mean radius is again 0.17 mm, and taking the geometric mean, we again find a mean crack radius of 0.36 mm. All of the crack size estimates for both cases are exceptionally close, and also close to the range of Darley Dale sandstone grain sizes. This strongly suggests that the crack size during crack growth is determined by the grain size. This is entirely as expected since the grain size is the only internal length scale available to provide such a constraint.

Taken together, these results show that although the number of cracks formed in the conventional triaxial test is much greater than that in the true triaxial test, the size of the cracks formed is essentially the same.

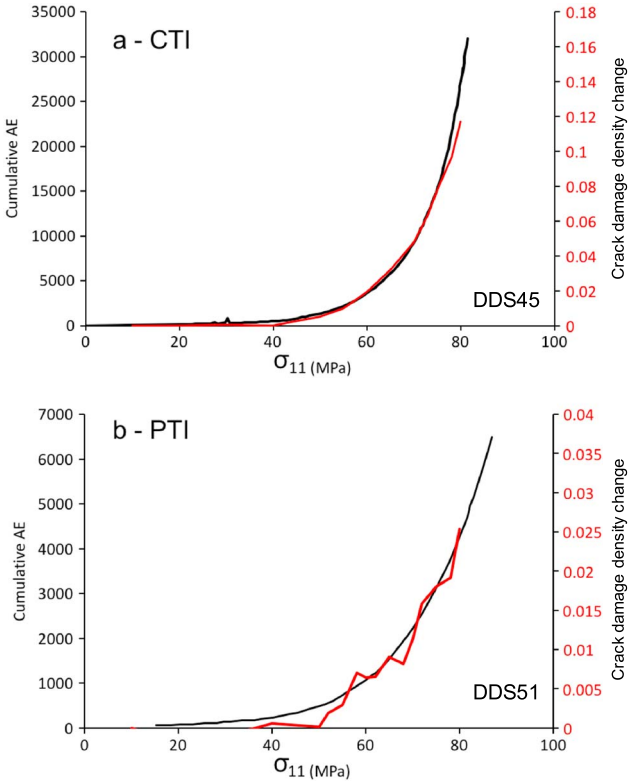

Figure 13. Calculated variation in density of dilatant cracks (with minor axes in σ_{33}) during a conventional triaxial test (a) creating CTI crack distributions and a true triaxial compression test (b) creating PTI crack distributions. Crack density is plotted with cumulative acoustic emission (AE) hits. Note the close similarity in the shape of the curves.

We suggest that this observation is fundamental to understanding rock strength under differing triaxial stress states. Triaxial strength is defined as the peak differential stress that can be sustained by a rock prior to failure [e.g., *Lockner*, 1993]. In the brittle field, macroscopic failure is driven by the coalescence of many microcracks to form a throughgoing fault [e.g., *Paterson and Wong*, 2005]. This crack coalescence is marked by strain weakening behavior, which starts near the peak stress and is a manifestation of intense damage generation and localization around the eventual fault plane [*Lockner et al.*, 1977]. Hence, ultimate failure commonly occurs after some period of weakening following the peak stress. Furthermore, earlier studies of brittle rock failure under both uniaxial [*Kranz and Scholz*, 1977] and conventional triaxial [*Baud and Meredith*, 1997; *Heap et al.*, 2009b, 2011] loading have shown that for any specific rock, the onset of strain weakening and acceleration toward failure occurs at the same critical level of crack damage regardless of the deformation rate or time-to-failure. Our wave velocity measurements and calculations of crack densities and sizes all indicate that relative to the conventional triaxial case where $\sigma_2 = \sigma_3$, the amount of crack damage is suppressed under true triaxial stress where $\sigma_2 > \sigma_3$ and is also restricted to the planes normal or subnormal to σ_3. So while we have not directly measured rock strength in our tests, our data elude to the mechanical control of the intermediate principal stress in suppressing the formation of microcracks leading to localization and failure [*Reches and Dieterich*, 1983]. This is illustrated in Figure 14 where we provide a comparison of strain and velocity data from conventional triaxial (CT) and true triaxial (TT) experiments. Figure 14a shows that the axial strain evolves broadly similarly with differential stress for the two cases, as expected, and within the range of sample variability. By contrast, the lateral strains evolve very differently. The lateral strain for the CT case exhibits significant dilatancy, whereas the lateral strains for the TT case (ε_{22} and ε_{33}) do not. ε_{33} tracks the CT lateral strain up to 40 MPa but exhibits only minor dilatancy at higher stress. Most importantly, the TT strain parallel to σ_{22} (ε_{22}) shows no dilatancy at any point. These observations are reflected in the volumetric strains, with significant net dilatancy in the CT case and no net dilatancy in the TT case. The changes in *P* wave velocities for the same experiment, shown in Figure 14b, are entirely consistent with the strain data. Apart from V_{22}, all the lateral velocities exhibit an increase due to initial net compaction followed by a decrease due to net dilatancy at higher differential stress. By contrast V_{22} always increases regardless of the stress level. Taken together, these data suggest that elevating σ_{22} above σ_{33} not only suppresses cracking along the σ_{22} axis but also decreases the amount of new crack damage generated along the σ_{33} axis.

If a critical level of crack damage is required to initiate failure, then our observations support the idea that the intermediate principal stress plays a crucial role in triaxial rock strength. This role being that as the intermediate principal stress is increased, significantly higher differential stresses are required to reach the level of

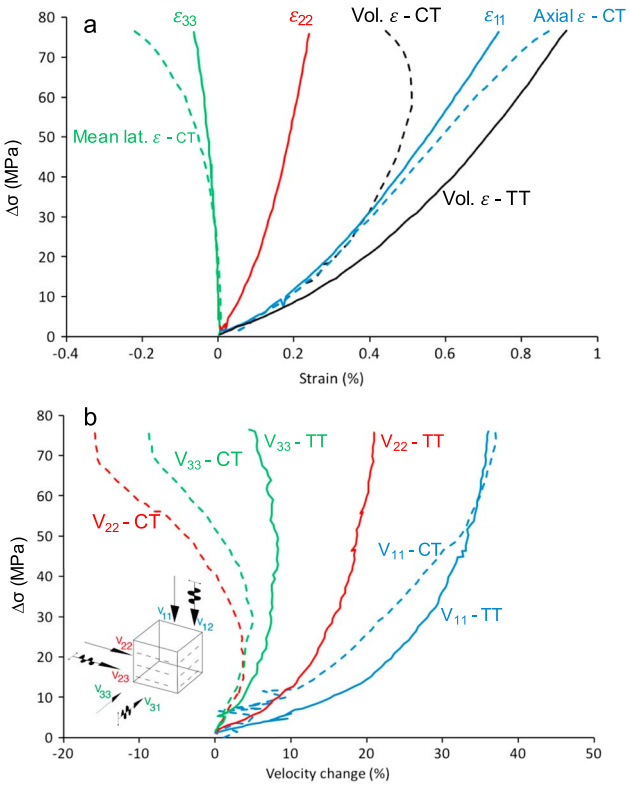

Figure 14. Comparison of strain and *P* wave velocity data for the conventional and true triaxial cases. (a) Variation in strain in all orientations for conventional (dashed lines) and true triaxial (solid lines) deformation as a function of differential stress. (b) Variation in *P* wave velocities in all orientations for the conventional (dashed lines) and true triaxial (solid lines) deformation as a function of differential stress.

damage needed to induce failure [*Haimson and Chang*, 2000; *Haimson*, 2006] because crack damage is suppressed in orientations not normal to σ_3. However, we should also note that in reality, the failure process may be even more complicated because it is likely not only to depend on the level of damage but also on its spatial distribution and clustering [*Kachanov and Sevostianov*, 2012].

4.4. Implications for Crack Damage Evolution During Both Loading and Unloading

As the crack distributions in our deformed sandstone have been shown to be anisotropic, it is not possible to visualize the full three-dimensional damage surface (set of damage envelopes) in deviatoric stress space because it is a six-dimensional property [*Holcomb and Costin*, 1986; *Murakami et al.*, 1998]. However, we can illustrate the effect of different loading regimes and stress states on damage envelope evolution via a Mohr-Coulomb construction (Figure 15) and also in mean stress $(\overline{\sigma})$ versus differential stress $(\Delta\sigma)$ space (cf. *P-Q* space) [*Cuss et al.*, 2003] (Figure S2).

We use the same data from the conventional triaxial stress test in section 3.3 (Figure 9) but with the load paths now plotted as $\overline{\sigma}$ and $\Delta\sigma$ for clarity of discussion (Figure 15a). Mohr-Coulomb constructions were plotted from the mean stress and differential stress states resulting from the same test and are shown in Figures 15b and 15c.

The zero (starting) stress state is isotropic, with $\sigma_{11} = \sigma_{22} = \sigma_{33} = 4$ MPa. The sample is then loaded differentially, with σ_{11} increased at a faster rate than σ_{22} and σ_{33}. The first key stress state (state (1) on Figure 15a) occurs with the onset of AE around 1800 s. This marks the nucleation of new, inelastic crack damage at a differential stress, $\Delta\sigma$, of 42 MPa ($\sigma_{11} = 52$ MPa, $\sigma_{22} = \sigma_{33} = 10$ MPa) and a mean stress, $\overline{\sigma}$, of 24 MPa. We therefore draw a crack damage envelope (Damage Envelope 1) in Figure 14a that is tangential to the Mohr stress circle for this stress state and tracks the Coulomb failure envelope (determined from the data of *Baud et al.* [2004]), as hypothesized by *Murrel* [1990]. The loading continues at the same rate to stress state (2) where $\Delta\sigma = 76$ MPa ($\sigma_{11} = 92$ MPa and $\sigma_{22} = \sigma_{33} = 15$ MPa) and $\overline{\sigma} = 41$ MPa. During this phase of increasing differential stress, we observe an accelerating rate of AE output, indicating an accelerating rate of new crack damage. We hypothesize that this increase in damage state pushes the damage envelope upward closer to the Coulomb failure line, and we therefore draw a tentative second damage envelope (Damage Envelope 2) in Figure 15b (dashed line), tangential to the new Mohr circle, at this point. Next, σ_{22} and σ_{33} are both increased to 30 MPa while σ_{11} is maintained constant at 92 MPa. This results in an increasing mean stress, $\overline{\sigma}$, but a decreasing differential stress, $\Delta\sigma$. The key observation here is that as soon as $\Delta\sigma$ starts to decrease there is an immediate cessation of all AE activity, indicating a complete shutdown of new damage, even though $\overline{\sigma}$ is increasing. At the end of this loading phase, $\Delta\sigma = 62$ MPa and $\overline{\sigma} = 51$ MPa, and this is plotted as stress state (3) in Figures 15b and 15c. We then entirely reverse the process by decreasing σ_{22}

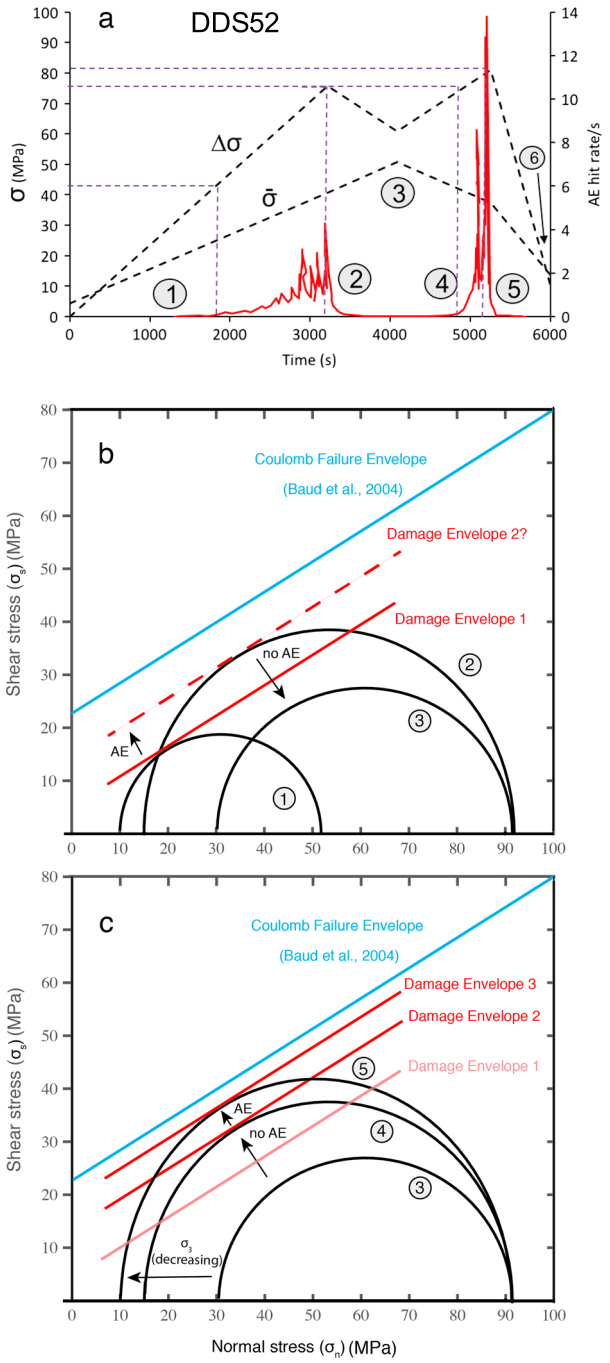

Figure 15. (a) Cyclic loading test plotted to show mean stress and differential stress. Mohr-Coulomb construction displaying stress states (b) 1–3 and (c) 3–5 as explained in text. Sufficient increases in differential stress generate acoustic emissions and therefore new crack damage. Further crack damage is only generated when the previous *damage envelope* is surpassed, a manifestation of the "Kaiser effect."

and σ_{33} while still maintaining σ_{11} constant at 92 MPa, so that $\Delta\sigma$ is increasing while $\bar{\sigma}$ is actually decreasing. A key observation is that following this stress path we cross Damage Envelope 1 entirely aseismically (Figure 15c). However, we observe that AE recommences when we reach stress state (4) in Figure 15c, and we note that this is exactly the same as stress state (2) in Figure 14b. So we observe a perfect manifestation of our concept of the Kaiser stress-memory effect: with AE recommencing when we reach Damage Envelope 2 and exceed the previous maximum *differential stress*, regardless of the level of σ_{11} or the mean stress. This confirms our earlier hypothesis that the damage envelope is dynamic and can be pushed closer to the failure envelope during cyclic loading (for a similar observation during uniaxial cyclic loading, see *Heap et al.* [2009a]). We continue decreasing σ_{22} and σ_{33} until we reach stress state (5) where $\Delta\sigma$ reaches its maximum value in this test of 82 MPa (σ_{11} = 92 MPa, $\sigma_{22} = \sigma_{33}$ = 10 MPa) and $\bar{\sigma}$ = 37 MPa. We note that there is a massive acceleration in AE output between stress states (4) and (5), and the damage envelope is hence pushed even closer to the failure envelope. We therefore draw Damage Envelope 3 at this point. Finally, we unloaded the sample by decreasing σ_{11} while maintaining σ_{22} and σ_{33} constant, resulting in a decrease in both $\Delta\sigma$ and $\bar{\sigma}$. Once again, this decrease in differential stress resulted in an immediate cessation of AE activity.

The loading and unloading tests have shown that while an individual stress state is important, the stress path by which this stress state is reached is equally important. Furthermore, whether that stress state has been "visited" before or not is also vitally important in terms of determining and understanding damage states. We therefore suggest that the description of the Kaiser effect as a stress-memory effect is potentially misleading and it should rather be described as a damage memory effect.

5. Conclusion

Measurement of the acoustic *P* and *S* wave velocities in three orthogonal directions show that

1. the wave velocity in a given direction increases with compressive stress in that direction, and this can be interpreted to give the change in crack density due to elastic deformation of cracks;
2. the wave velocity in the direction of the minimum principal stress decreases at differential stresses above the value at which new crack damage is initiated. Thus, significant anisotropy of the crack population develops in response to the application of differential stresses, independent of the mean stress. This can only be fully observed under truly triaxial conditions.

Acoustic emission (AE) can be used to evaluate the onset and evolution of new crack damage caused by inelastic processes in rocks under both conventional and true traixial loading conditions. By comparing acoustic emissions and crack densities from conventional triaxial tests and true triaxial tests we have further shown how the intermediate principal stress plays a key role in inhibating crack damage. The differential stress under which the initial formation of cracks occurs was determined in our tests. We have shown that the formation of crack damage can be generated through reduction in minimum principal stress which increases differential stress regardless of the mean stress state. This implies that crack damage in fault zones can increase during unloading. We have shown that crack damage evolution can be anisotropic and must be considered as a three-dimensional problem. Future studies should consider this problem under truly triaxial conditions and further consider saturated conditions and effects on permeability.

Acknowledgments

We thank the Associate Editor, Michelle Cooke, and the reviewers, Ze'ev Reches and Yves Guéguen, for useful comments which helped to improve the manuscript. We thank J.G. Van Munster for providing access to the true triaxial apparatus at KSEPL and for technical support during the experimental program. We thank R. Pricci for assistance with technical drawings of the apparatus. This work was partly funded by NERC award NE/N002938/1 and by a NERC Doctoral Studentship, which we gratefully acknowledge. Supporting data are included in a supporting information file; any additional data may be obtained from J.B. (e-mail: j.browning@ucl.ac.uk).

References

Anderson, D. L., B. Minster, and D. Cole (1974), The effect of oriented cracks on seismic velocities, *J. Geophys. Res.*, *79*, 4011–4015, doi:10.1029/JB079i026p04011.

Ayling, M. R., P. G. Meredith, and S. A. Murrell (1995), Microcracking during triaxial deformation of porous rocks monitored by changes in rock physical properties, I. Elastic-wave propagation measurements on dry rocks, *Tectonophysics*, *245*, 205–221.

Baud, P., and P. G. Meredith (1997), Damage accumulation during triaxial creep of Darley Dale sandstone from pore volumometry and acoustic emission, *Int. J. Rock Mech. Min. Sci.*, *34*, 24.e1–24.e10.

Baud, P., E. Klein, and T. F. Wong (2004), Compaction localization in porous sandstones: Spatial evolution of damage and acoustic emission activity, *J. Struct. Geol.*, *26*, 603–624.

Baud, P., P. Meredith, and E. Townend (2012), Permeability evolution during triaxial compaction of an anisotropic porous sandstone, *J. Geophys. Res.*, *117*, B05203, doi:10.1029/2012JB009176.

Brantut, N. (2015), Time-dependent recovery of microcrack damage and seismic wave speeds in deformed limestone, *J. Geophys. Res. Solid Earth*, *120*, 8088–8109, doi:10.1002/2015JB012324.

Cox, S. J. D., and P. G. Meredith (1993), Microcrack formation and material softening in rock measured by monitoring acoustic emissions, *Int. J. Rock Mech. Min. Sci. Geomech. Abstr.*, *30*, 11–24.

Crawford, B. R., B. G. D. Smart, I. G. Main, and F. Liakopoulou-Morris (1995), Strength characteristics and shear acoustic anisotropy of rock core subjected to true triaxial compression, *Int. J. Rock Mech. Min. Sci. Geomech. Abstr.*, *32*, 189–200.

Cuss, R. J., E. H. Rutter, and R. F. Holloway (2003), The application of critical state soil mechanics to the mechanical behaviour of porous sandstones, *Int. J. Rock Mech. Min. Sci.*, *40*, 847–862.

Ghaffari, H. O., M. H. B. Nasseri, and R. P. Young (2014), Faulting of rocks in a three-dimensional stress field by micro-anticracks, *Sci. Rep.*, *4*, 5011, doi:10.1038/srep05011.

Guéguen, Y., and M. Kachanov (2011), Effective elastic properties of cracked rocks—An overview, in *In Mechanics of Crustal Rocks*, pp. 73–125, Springer, Vienna.

Hackston, A., and E. Rutter (2016), The Mohr–Coulomb criterion for intact rock strength and friction—A re-evaluation and consideration of failure under polyaxial stresses, *Solid Earth*, *7*, 493–508.

Hadley, K. (1976), Comparison of calculated and observed crack densities and seismic velocities in Westerly granite, *J. Geophys. Res.*, *81*, 3484–3494, doi:10.1029/JB081i020p03484.

Haimson, B. (2006), True triaxial stresses and the brittle fracture of rock, in *In Rock Damage and Fluid Transport, Part I*, pp. 101–1130, Birkhäuser, Basel, Switzerland.

Haimson, B., and C. Chang (2000), A new true triaxial cell for testing mechanical properties of rock, and its use to determine rock strength and deformability of Westerly granite, *Int. J. Rock Mech. Min. Sci.*, *37*, 285–296.

Han, T. (2016), A simple way to model the pressure dependency of rock velocity, *Tectonophysics*, *675*, 1–6.

Healy, D., T. G. Blenkinsop, N. E. Timms, P. G. Meredith, T. M. Mitchell, and M. L. Cooke (2015), Polymodal faulting: Time for a new angle on shear failure, *J. Struct. Geol.*, *80*, 57–71.

Heap, M. J., S. Vinciguerra, and P. G. Meredith (2009a), The evolution of elastic moduli with increasing crack damage during cyclic stressing of a basalt from Mt. Etna volcano, *Tectonophysics*, *471*, 153–160.

Heap, M. J., P. Baud, P. G. Meredith, A. F. Bell, and I. G. Main (2009b), Time-dependent brittle creep in Darley Dale sandstone, *J. Geophys. Res.*, *114*, B07203, doi:10.1029/2008JB006212.

Heap, M. J., P. Baud, P. G. Meredith, S. Vinciguerra, A. F. Bell, and I. G. Main (2011), Brittle creep in basalt and its application to time-dependent volcano deformation, *Earth Planet. Sci. Lett.*, *307*, 71–82.

Hoenig, A. (1979), Elastic moduli of a non-randomly cracked body, *Int. J. Solids Struct.*, *15*, 137–154.

Holcomb, D. J. (1993), General theory of the Kaiser effect, *Int. J. Rock Mech. Min. Sci. Geomech. Abstr.*, *30*(7), 929–935.

Holcomb, D. J., and L. S. Costin (1986), Detecting damage surfaces in brittle materials using acoustic emissions, *J. Appl. Mech.*, *53*, 536–544.

Ingraham, M. D., K. A. Issen, and D. J. Holcomb (2013), Use of acoustic emissions to investigate localization in high-porosity sandstone subjected to true triaxial stresses, *Acta Geotech.*, *8*, 645–663.
Kachanov, M. (1992), Effective elastic properties of cracked solids: Critical review of some basic concepts, *Appl. Mech. Rev.*, *45*, 304–335.
Kachanov, M., and I. Sevostianov (2012), Rice's internal variables formalism and its implications for the elastic and conductive properties of cracked materials, and for the attempts to relate strength to stiffness, *J. Appl. Mech.*, *79*, 31002.
Kranz, R. L., and C. H. Scholz (1977), Critical dilatant volume of rocks at the onset of tertiary creep, *J. Geophys. Res.*, *82*, 4893–4898, doi:10.1029/JB082i030p04893.
Lavrov, A. (2001), Kaiser effect observation in brittle rock cyclically loaded with different loading rates, *Mech. Mater.*, *33*, 669–677.
Lockner, D. (1993), The role of acoustic emission in the study of rock fracture, *Int. J. Rock Mech. Min. Sci. Geomech..*, *30*(7), 883–899.
Lockner, D. A., J. B. Walsh, and J. D. Byerlee (1977), Changes in seismic velocity and attenuation during deformation of granite, *J. Geophys. Res.*, *82*, 5374–5378, doi:10.1029/JB082i033p05374.
McLaskey, G. C., and D. A. Lockner (2014), Preslip and cascade processes initiating laboratory stick slip, *J. Geophys. Res. Solid Earth*, *119*, 6323–6336, doi:10.1002/2014JB011220.
Murakami, S., K. Hayakawa, and Y. Liu (1998), Damage evolution and damage surface of elastic-plastic-damage materials under multiaxial loading, *Int. J. Damage Mech.*, *7*, 103–128.
Murrel, S. A. F. (1990), Brittle-to-ductile transitions in polycrystalline non-metallic materials, in *Deformation Processes in Minerals, Ceramics and Rocks*, vol. 1, edited by D. J. Barber and P. G. Meredith, pp. 109–137, Min. Soc. Great Britain and Ireland, London.
Nasseri, M. H. B., S. D. Goodfellow, L. Lombos, and R. P. Young (2014), 3-D transport and acoustic properties of Fontainebleau sandstone during true-triaxial deformation experiments, *Int. J. Rock Mech. Min. Sci.*, *69*, 1–18.
Nur, A., and G. Simmons (1969), Stress-induced velocity anisotropy in rock: An experimental study, *J. Geophys. Res.*, *74*, 6667–6674, doi:10.1029/JB074i027p06667.
Nye, J. F. (1957), *Physical Properties of Crystals*, Clarendon, Oxford.
Paterson, M. S., and T. F. Wong (2005), *Experimental Rock Deformation—The Brittle Field*, Springer Science & Business Media, Berlin.
Reches, Z. E., and J. H. Dieterich (1983), Faulting of rocks in three-dimensional strain fields I. Failure of rocks in polyaxial, servo-control experiments, *Tectonophysics*, *95*, 111–132.
Sayers, C. M., and M. Kachanov (1995), Microcrack-induced elastic wave anisotropy of brittle rocks, *J. Geophys. Res.*, *100*, 4149–4156, doi:10.1029/94JB03134.
Sayers, C. M., and J. G. Van Munster (1991), Microcrack-induced seismic anisotropy of sedimentary rocks, *J. Geophys. Res.*, *96*, 16,529–16,533, doi:10.1029/91JB01232.
Sayers, C. M., J. G. Van Munster, and M. S. King (1990), Stress-induced ultrasonic anisotropy in Berea sandstone, *Int. J. Rock Mech. Min. Sci. Geomech. Abstr.*, *27*(5), 429–436.
Schubnel, A., O. Nishizawa, K. Masuda, X. J. Lei, Z. Xue, and Y. Guéguen (2003), Velocity measurements and crack density determination during wet triaxial experiments on Oshima and Toki granites, in *In Thermo-Hydro-Mechanical Coupling in Fractured Rock*, pp. 869–887, Birkhäuser, Basel, Switcerland.
Schubnel, A., P. M. Benson, B. D. Thompson, J. F. Hazzard, and R. P. Young (2006), Quantifying damage, saturation and anisotropy in cracked rocks by inverting elastic wave velocities, *Pure Appl. Geophys.*, *163*, 947–973.
Shi, L., X. Li, B. Bai, Q. Li, and X. Feng (2012), Numerical analysis of loading boundary effects in Mogi-type true triaxial tests, in *True Triaxial Testing of Rocks*, edited by M. Kwasniewski, X. Li, and M. Takahashi, pp. 19–34, CRC Press, Leiden, Netherlands.
Soga, N., H. Mizutani, H. Spetzler, and R. J. Martin (1978), The effect of dilatancy on velocity anisotropy in Westerly granite, *J. Geophys. Res.*, *83*, 4451–4458, doi:10.1029/JB083iB09p04451.
Stuart, C. E. (1992), Evolution of anisotropic microcrack damage in cyclically stressed rock, characterized by contemporaneous acoustic emission and elastic wave velocity measurements, Unpublished thesis, Univ. of London.
Stuart, C. E., P. G. Meredith, S. A. F. Murrell, and J. G. Van Munster (1993), Anisotropic crack damage and stress-memory effects in rocks under triaxial loading, *Int. J. Rock Mech. Min. Sci. Geomech. Abstr.*, *30*(7), 937–941.
Stuart, C. E., P. G. Meredith, S. A. F. Murrell, and H. Van Munster (1995), Influence of anisotropic crack damage development on the Kaiser effect under true triaxial stress conditions, *Ser. Rock Soil Mech.*, *19*, 205–220.
Thomsen, L. (1986), Weak elastic anisotropy, *Geophysics*, *51*, 1954–1966.
Wibberley, C. A. J., J. P. Petit, and T. Rives (2007), The mechanics of fault distribution and localization in high-porosity sands, Provence, France, *Geol. Soc. London Spec. Publ.*, *289*, 19–46.
Wu, X. Y., P. Baud, and T. F. Wong (2000), Micromechanics of compressive failure and spatial evolution of anisotropic damage in Darley Dale sandstone, *Int. J. Rock Mech. Min. Sci.*, *37*, 143–160.
Zoback, M. D., and M. L. Zoback (2002), State of stress in the Earth's lithosphere, *Int. Geophys.*, *81*, 559–XII.